Draft version December 2, 2015
Preprint typeset using LaTeX style emulateapj v. 01/23/15

arXiv:1512.00386v1 [astro-ph.IM] 1 Dec 2015

RELATIVISTIC HYDRODYNAMICS WITH WAVELETS

Jackson DeBuhr, Bo Zhang, Matthew Anderson
Center for Research in Extreme Scale Technologies, School of Informatics and Computing, Indiana University, Bloomington, IN 47404
and
David Neilsen, Eric W. Hirschmann
Department of Physics and Astronomy, Brigham Young University, Provo, UT 84602
Draft version December 2, 2015

ABSTRACT

Methods to solve the relativistic hydrodynamic equations are a key computational kernel in a large number of astrophysics simulations and are crucial to understanding the electromagnetic signals that originate from the merger of astrophysical compact objects. Because of the many physical length scales present when simulating such mergers, these methods must be highly adaptive and capable of automatically resolving numerous localized features and instabilities that emerge throughout the computational domain across many temporal scales. While this has been historically accomplished with adaptive mesh refinement (AMR) based methods, alternatives based on wavelet bases and the wavelet transformation have recently achieved significant success in adaptive representation for advanced engineering applications. This work presents a new method for the integration of the relativistic hydrodynamic equations using iterated interpolating wavelets and introduces a highly adaptive implementation for multidimensional simulation. The wavelet coefficients provide a direct measure of the local approximation error for the solution and place collocation points that naturally adapt to the fluid flow while providing good conservation of fluid quantities. The resulting implementation, oahu, is applied to a series of demanding one- and two-dimensional problems which explore high Lorentz factor outflows and the formation of several instabilities, including the Kelvin-Helmholtz instability and the Rayleigh-Taylor instability.

Keywords: wavelets, relativistic hydrodynamics

1. INTRODUCTION

Relativistic fluids are used to model a variety of systems in high-energy astrophysics, such as neutron stars, accretion onto compact objects, supernovae, and gamma-ray burst outflows. Consequently, methods to solve the relativistic hydrodynamic equations are a key scientific kernel in a large number of astrophysics simulations and toolkits. Because of the many physical length scales present when simulating astrophysical phenomena, these methods must also be highly adaptive and capable of automatically resolving many localized emerging features and instabilities throughout the computational domain across many temporal scales. For Eulerian fluid methods, this has been historically accomplished with adaptive mesh refinement (AMR) based methods (Berger and Oliger 1984; Anderson et al. 2006). Other approaches include smoothed particle hydrodynamics (Rosswog 2010), and solving the fluid equations on a moving Voronoi mesh (Springel 2010; Duffell and MacFadyen 2011). Alternative methods based on wavelets and the wavelet transformation have recently achieved significant success in adaptive representation for advanced engineering applications (Paolucci et al. 2014a, Paolucci et al. 2014b). This has inspired and encouraged their investigation and possible application in relativistic hydrodynamics. This work presents a new method for the integration of the relativistic hydrodynamic equations using iterated interpolating wavelets and introduces a highly adaptive implementation for multidimensional simulations called oahu.

The merger of two neutron stars or a black hole and a neutron star is an astrophysical system that has attracted significant interest. The orbital motion of the compact objects generates gravitational waves that are likely to be observed in the new Advanced-LIGO class of gravitational wave detectors. When operating at design sensitivity, these detectors are expected to make many detections of gravitational wave events each year (Abadie et al. 2010). These binaries are also expected to be sources of significant electromagnetic emission, such as magnetosphere interactions that give a precursor signal to merger (Palenzuela et al. 2013), kilonova events from r-process reactions on the neutron-rich ejecta (Li and Paczynski 1998), and short gamma-ray bursts (SGRBs) (Berger 2013). The combination of gravitational wave and electromagnetic observations, known as multi-messenger astronomy, should open new insights into some important questions, such as fundamental tests of general relativity, the neutron star equation of state, the earliest stages of supernova explosions, and models for GRB progenitors.

Computational models of neutron star binary mergers, when compared with observational data, are giving additional insights into such systems. For example, a black hole-neutron star merger can produce enough ejecta to power an SGRB, but only if the black hole has a small mass or a high spin (Chawla et al. 2010; Foucart et al. 2013). Moreover, simulations of neutron star binaries with a soft equation of state produce sufficient ejecta to power an SGRB through accretion, while those with

{jdebuhr,zhang416,andersmw}@indiana.edu
{david.neilsen,ehirsch}@physics.byu.edu

a stiff equation of state produce much less ejecta (Hotokezaka et al. 2013; Sekiguchi et al. 2015; Palenzuela et al. 2015). Given this evidence from computer simulations, it appears that binary neutron star mergers and a softer nuclear equation of state may be preferred for the production of SGRBs. However, this continues to be an active area of research, and we expect these results to be refined as more results become available.

Computer models of neutron star binaries can be challenging to perform. On one hand, these models require a considerable amount of sophisticated physics to be realistic. Such models should include full general relativity for the dynamic gravitational field, a relativistic fluid model that includes a magnetic field (e.g. ideal or resistive magnetohydrodynamics), a finite-temperature equation of state for the nuclear matter, and a radiation hydrodynamics scheme for neutrinos. All of these components must be robust and work for a large range of energies. A second challenge, alluded to above, is the large range of scales that must be resolved. The neutron star radius sets one scale, 10–15 km, as the star must be well resolved on the computational domain. Other length scales are set by the orbital radius, 50–100 km, and the gravitational wave zone, approximately 100–1,000 km. Furthermore, some fluid instabilities can significantly increase the magnetic field strength in the post-merger remnant, making resolutions on the scale of meters advantageous (Kiuchi et al. 2014). Finally, the computer models need to run efficiently on modern high performance computers, requiring them to be highly parallelizable and scalable to run on thousands of computational cores.

We are developing the OAHU code to address the challenge of simulating binary mergers with neutron stars. A key component of this code is that we combine a robust high-resolution shock-capturing method with an unstructured dyadic grid of collocation points that conforms to the features of the solution. This grid adaptivity is realized by expanding functions in a wavelet basis and adding refinement only where the solution has small-scale features.

Wavelets allow one to represent a function in terms of a set of basis functions which are localized both spatially and with respect to scale. In comparison, spectral bases are infinitely differentiable, but have global support; basis functions used in finite difference or finite element methods have small compact support, but poor continuity properties. Wavelets with compact support have been applied to the solutions of elliptic, parabolic, and hyperbolic PDEs (Beylkin 1992; Beylkin and Coult 1998; Alpert et al. 2002; Qian and Weiss 1993a,b; Latto and Tenenbaum 1990; Glowinski et al. 1989; Holmström 1999; Dahmen et al. 1997; Urban 2009; Alam et al. 2006; Chegini and Stevenson 2011). Wavelets have also been applied to the solutions of integral equations (Alpert et al. 1993). We note that when applied to nonlinear equations, some of these previous methods will map the space of wavelet coefficients onto the physical space and there compute the nonlinear terms. They then project that result back to the wavelet coefficients space using analytical quadrature or numerical integration. Our approach is rather to combine collocation methods with wavelets thus allowing us to operate in a single space (Bertoluzza and Naldi 1996; Vasilyev and Bowman 2000; Regele and Vasilyev 2009; Vasilyev et al. 1995; Vasilyev and Paolucci 1996, 1997).

In astronomy, wavelets have seen extensive use in analysis tasks, from classifying transients (Powell et al. 2015; Varughese et al. 2015), to image processing (Mertens and Lobanov 2015), and to finding solutions to nonlinear initial value problems (Kazemi Nasab et al. 2015). They have not, however, seen much use in solutions of PDEs in astrophysics.

This paper reports on an initial version of OAHU that implements the first two elements above, concentrating on the initial tests of the fluid equations and adaptive wavelet grid. A discussion of the Einstein equation solver and parallelization will be presented in subsequent papers. The organization of this paper is as follows. In section 2 we describe our model system and the numerical methods used. Section 3 presents one dimensional tests of the resulting scheme. In section 4 we present the results of applying the method to the relativistic Kelvin-Helmholtz instability. Section 5 presents a stringent test of our method as applied to a relativistic outflow that develops Rayleigh-Taylor generated turbulence. Finally, in section 6 we summarize results and make note of future work suggested by the method.

2. METHODS

This section describes some of the numerical approaches and algorithms used in OAHU.

2.1. *Relativistic Hydrodynamics*

In general relativity the spacetime geometry is described by a metric tensor $g_{\mu\nu}$, and we write the line element in ADM form as

$$\mathrm{d}s^2 = g_{\mu\nu}\,\mathrm{d}x^\mu \mathrm{d}x^\nu \tag{1}$$

$$= (-\alpha^2 + \beta_i\beta^i)\,\mathrm{d}t^2 + 2\beta_i\,\mathrm{d}t\mathrm{d}x^i + \gamma_{ij}\,\mathrm{d}x^i\mathrm{d}x^j. \tag{2}$$

We write these equations in units where the speed of light is set to unity, $c = 1$. Repeated Greek indices sum over all spacetime coordinates, $0, 1, 2, 3$, and repeated Latin indices sum over the spatial coordinates, $1, 2, 3$. α and β^i are functions that specify the coordinates and γ_{ij} is the 3-metric on spacelike hypersurfaces. While our code is written for a completely generic spacetime, the tests presented in this paper are all performed in flat spacetime. To simplify the presentation, we write the equations in special relativity (i.e. flat spacetime) in general curvilinear coordinates, and we set $\alpha = 1$ and $\beta^i = 0$. In Cartesian coordinates, the flat space metric is the identity $\gamma_{ij} = \mathrm{diag}(1, 1, 1)$, but γ_{ij} is generally a function of the curvilinear coordinates.

A perfect fluid in special relativity is described by a stress-energy tensor of the form

$$T_{\mu\nu} = hu_\mu u_\nu + Pg_{\mu\nu}\,, \tag{3}$$

where h is the total enthalpy of the fluid

$$h = \rho(1 + \varepsilon) + P. \tag{4}$$

The fluid variables ρ, ε, u^μ, and P are the rest mass density, the specific internal energy, the four-velocity and the pressure of the fluid, respectively. Once an equation of state of the form $P = P(\rho, \varepsilon)$ is adopted, the equations determining the matter dynamics are obtained from the conservation law $\nabla_\mu T^\mu{}_\nu = 0$ and the conservation of baryons $\nabla_\mu(\rho u^\mu) = 0$.

We introduce the three-velocity of the fluid, v^i, and the Lorentz factor W by writing the four-velocity as

$$u^\mu = (W, Wv^i)^T. \tag{5}$$

The four-velocity has a fixed magnitude $u_\mu u^\mu = -1$, which gives the familiar relation between W and v^i

$$W^2 = \frac{1}{1 - v_i v^i}. \tag{6}$$

We introduce a set of *conservative* variables

$$\tilde{D} \equiv \sqrt{\gamma}\rho W \tag{7}$$

$$\tilde{S}_i \equiv \sqrt{\gamma}\left(hW^2 v_i\right) \tag{8}$$

$$\tilde{\tau} \equiv \sqrt{\gamma}\left(hW^2 - P - \rho W\right). \tag{9}$$

These quantities correspond in the Newtonian limit to the rest mass density, the momentum, and the kinetic energy of the fluid, respectively. A tilde ($\tilde{}$) indicates that each quantity has been *densitized* by the geometric factor $\sqrt{\gamma}$, where $\gamma = \det\gamma_{ij}$. In terms of these fluid variables, the relativistic fluid equations are

$$\partial_t \tilde{D} + \partial_i\left(\tilde{D}v^i\right) = 0 \tag{10}$$

$$\partial_t \tilde{S}_j + \partial_i\left(v^i \tilde{S}_j + \sqrt{\gamma}P\gamma^i{}_j\right) = {}^3\Gamma^i{}_{kj}\left(v^k \tilde{S}_i + \sqrt{\gamma}P\gamma^k{}_i\right) \tag{11}$$

$$\partial_t \tilde{\tau} + \partial_i\left(\tilde{S}^i - \tilde{D}v^i\right) = 0, \tag{12}$$

where ${}^3\Gamma^i{}_{jk}$ are the Christoffel symbols associated with the spatial metric γ_{ij}.

The fluid equations of motion can be written in balance law form

$$\partial_t \mathbf{u} + \partial_i \mathbf{f}^i(\mathbf{u}) = \mathbf{s}(\mathbf{u}), \tag{13}$$

where $\mathbf{u}$ is the state vector of conserved variables and $\mathbf{f}^i$ are the fluxes

$$\mathbf{u} = \begin{pmatrix} \tilde{D} \\ \tilde{S}_i \\ \tilde{\tau} \end{pmatrix}, \qquad \mathbf{f}^i = \begin{pmatrix} \tilde{D}v^i \\ v^i \tilde{S}_j + \sqrt{\gamma}P\gamma^i{}_j \\ \tilde{S}^i - \tilde{D}v^i \end{pmatrix}. \tag{14}$$

The fluid equations in curvilinear coordinates have geometric source terms, which are included in $\mathbf{s}$.

Finally, the system of equations is closed with an equation of state. We use the Γ-law equation of state

$$P = (\Gamma - 1)\rho\,\varepsilon, \tag{15}$$

where Γ is the adiabatic constant.

2.2. *Sparse Field Representation*

In this section we describe how we construct the sparse, adaptive representation of fields. The essential ingredients are the iterative interpolation of Deslauriers and Dubuc (1989) and the wavelet representation of Donoho (1992). This presentation follows that in Holmström (1999). We begin with the one dimensional case; see Section 2.3 for the generalization to higher dimensions.

The method begins with a nested set of dyadic grids, V_j (see Figure 1):

$$V_j = \left\{x^{j,k} : x^{j,k} = 2^{-j}k\Delta x\right\}. \tag{16}$$

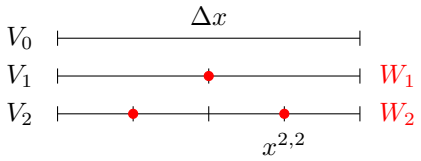

Figure 1. The one dimensional nested dyadic grids, V_j. This example has $N = 1$ and shows up to level $j = 2$. The point at $j = 2$, $k = 2$ is labeled. In red are shown those points that are part of the alternate grids, W_j, which are defined for $j > 1$.

Here Δx is the spacing at level $j = 0$, called the base level, and k is an integer indexing the points within the various grid levels. Notice that the points in V_j will also appear in all higher level grids V_l (where $l > j$). The points of even k at level j will also be in the grid at level $j-1$. If the overall domain size is L, and there are $N+1$ points in grid V_0, then $\Delta x = L/N$.

Starting with a set of field values at level j, $u^{j,k}$, we can extend these values to higher levels of the grid using interpolation. For those points in V_{j+1} that are also in V_j, we just copy the value from the coarser grid: $u^{j+1,2k} = u^{j,k}$. The previous is also the means by which the field values can be restricted to coarser levels: points at coarser levels have values copied from finer levels. For the points first appearing in grid V_{j+1} we take the nearest p field values from grid V_j and interpolate:

$$u^{j+1,2k+1} = \sum_m h^{j+1,2k+1}_{j,m} u^{j,m}. \tag{17}$$

Here $h^{l,m}_{j,k}$ are the coefficients for interpolation from level j to level l. In practice, for a given k, only a small number of these coefficients are nonzero. In this work we use $p = 4$, so we have

$$u^{j+1,2k+1} = -\frac{1}{16}u^{j,k-1} + \frac{9}{16}u^{j,k} + \frac{9}{16}u^{j,k+1} - \frac{1}{16}u^{j,k+2}. \tag{18}$$

The previous applies in the interior of the grid. Near the boundaries, little changes, except the nearest points are no longer symmetric around the refined point, and the coefficients in the sum are different. Having advanced the field values to grid V_{j+1}, the procedure can be iterated to advance the field to V_{j+2}. In this way, any level of refinement can be achieved from the initial sequence, and when performed *ad infinitum* produces a function on the interval $[0, L]$ (see Donoho (1992) for details about the regularity of these functions).

The linearity of this procedure suggests a natural set of basis functions for iterated interpolation functions formed from Kronecker sequences. That is, start with a sequence that has a single 1 at level j and interpolate, $\phi_{j,k}(x^{j,l}) = \delta^l_k$. The resulting function, $\phi_{j,k}(x)$ has a number of properties, among which is the two-scale relation:

$$\phi_{j,k}(x) = \sum_l c^l \phi_{j+1,l}(x). \tag{19}$$

One step of the interpolation will produce a sequence on V_{j+1}, which can be written as a weighted sum of the

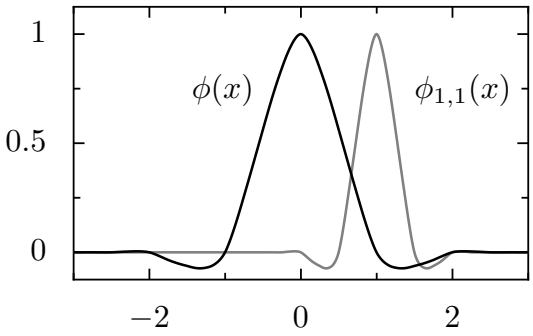

Figure 2. The fundamental solution of the iterated interpolation for $p = 4$, $\phi(x)$ (black) and a basis element in level one, $\phi_{1,1}(x)$ (gray). Each basis function is a scaled, translated version of the fundamental solution.

Kronecker sequences on V_{j+1}. Indeed, the weights c^l are easy to find from the interpolation. For $p = 4$ these are $c^l = \{..., 0, -1/16, 0, 9/16, 1, 9/16, 0, -1/16, 0, ...\}$. Each of these functions is a scaled, translated version of a single function $\phi(x)$, shown in Figure 2, called the fundamental solution of the interpolation: $\phi_{j,k}(x) = \phi(2^j x/\Delta x - k)$.

The previous functions can be used to form bases for each level of the grid separately. The two-scale relation prevents the full set from being a basis on the full set of collocation points. In particular, note that for each location in the grid, $x^{j,k}$ there is one such function. However, certain locations are represented on multiple levels, for example $x^{j,k} = x^{j+m,2^m k}$ for all $m > 0$. To form a basis for the full grid, introduce the alternate higher level grids, W_j, for $j > 0$:

$$W_j = \left\{ x^{j,k} : x^{j,k} = 2^{-j} k \Delta x,\ k \text{ odd} \right\}. \tag{20}$$

The W_j grids are the V_j grids with the points from earlier levels removed (see the red points in Figure 1). The set of grids $\{V_0, W_j\}$ now has each point represented exactly once. Forming a basis for these points is achieved by taking the set of $\phi_{j,k}(x)$ functions that correspond to the points in the base grid, and these higher level alternate grids, W_j. With this basis, we can represent a field, u, as follows:

$$u(x) = \sum_{k \in S_0} u^{0,k} \phi_{0,k}(x) + \sum_{j=1} \sum_{k \in S_j} d^{j,k} \phi_{j,k}(x). \tag{21}$$

where $S_0 = \{0, 1, ..., N\}$ is the index set for grid V_0 and $S_j = \{1, 3, ..., 2^j N - 1\}$ is the index set for grid W_j.

The previous is the interpolating wavelet expansion of the field. Intuitively, the expansion contains the coarse picture (level 0) and refinements of that picture at successively finer levels. The expansion coefficients $u^{0,k}$ are just the field values at the base level points: $u^{0,k} = u(x^{0,k})$. We can extend this notation to include $u^{j,k} = u(x^{j,k})$. The coefficients $d^{j,k}$, called *wavelet coefficients*, are computed by comparing the interpolation from the previous level to the field value, $u^{j,k}$. In particular if we denote the interpolated value from level j at a level $j+1$ point, $\tilde{u}^{j+1,k} = P(x^{j+1,k}, j)$, then

$$d^{j,k} = u^{j,k} - P(x^{j,k}, j-1). \tag{22}$$

Intuitively, the wavelet coefficient measures the failure of the field to be the interpolation from the previous level. The previous is also called the forward wavelet transformation. This transformation starts with field values on the multi-level grid, and produces wavelet coefficients. The transformation can be easily inverted by rearranging the equation, and computing field values given the wavelet coefficients.

There are two descriptions of the field on the multi-level grid. The first, called the *Point Representation* is the set of values $\{u^{j,k}\}$. The second, called the *Wavelet Representation* is the set of values $\{u^{0,k}, d^{j,k}\}$. These representations can be made sparse via thresholding. Starting with the Wavelet Representation, and given a threshold ϵ, the *Sparse Wavelet Representation* is formed by removing those points whose wavelet coefficient are below some threshold: $|d^{j,k}| < \epsilon$. This amounts to discarding those points that are well approximated by interpolation. This naturally cuts down the number of points in the grid, and introduces an *a priori* error bound (Donoho 1992) on the representation of the field. The points whose values are kept are called *essential* points. The level 0 points are always kept and are always essential. The field values at the essential points form the *Sparse Point Representation.*

2.3. *Higher Dimensions*

In multiple dimensions, the construction is not much more involved. The basis functions are taken to be the products of the 1-dimensional functions:

$$\phi_{j,\vec{k}}(x, y, z) = \phi_{j,k_x}(x) \phi_{j,k_y}(y) \phi_{j,k_z}(z). \tag{23}$$

In the previous, $\vec{k} = (k_x, k_y, k_z)$ is the set of three indices required to label a three dimensional grid (see Figure 3). Another way to construct these functions is by interpolation in multiple dimensions. Depending on the location of the level $j+1$ point in the level j grid, this interpolation will involve p, p^2 or p^3 terms (Figure 4). The wavelet coefficient for a point is again computed as the difference between the field value and the interpolated value, it is just that the interpolation often contains more terms.

The rest of the method goes through as one might expect. The field is expanded in terms of these basis functions:

$$u(x, y, z) = \sum_{\vec{k}} u^{0,\vec{k}} \phi_{0,\vec{k}}(x, y, z) + \sum_{j=1} \sum_{\vec{k}} d^{j,\vec{k}} \phi_{j,\vec{k}}(x, y, z). \tag{24}$$

The sparse representation is formed by removing those points whose wavelet coefficient have a magnitude less than the prescribed error threshold, ϵ.

2.4. *Conservation*

It is possible to measure the conservation of the fields being evolved using the wavelet basis. In particular, the quantity

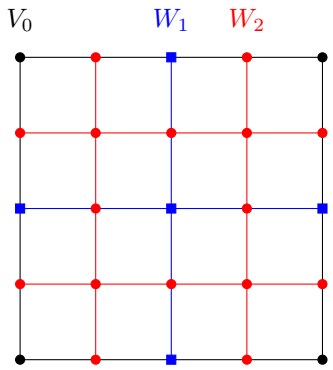

Figure 3. A slice of the 3d grid. The black points (circles) are those in the base grid, the blue points (squares) belong to level 1, and the red points (circles) belong to level 2. Notice that some points at level 1 line up with points at level 0, and that some points at level 2 line up with points at level 1.

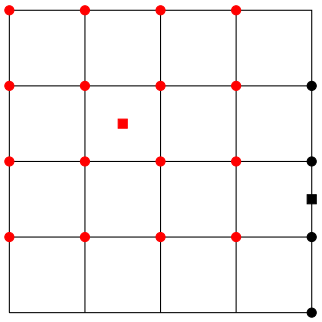

Figure 4. A portion of a slice of the 3d grid at level j. Shown are those points at level j (circles) that contribute to the wavelet transformation for the marked points at level $j+1$ (squares). Depending on the relative placement of the level $j+1$ points to the level j grid, the wavelet transformation will use p (black) or p^2 (red) points. In three dimensions this extends to cases that also use p^3 points.

$$\int_\Sigma u(x)dx, \tag{25}$$

where Σ is the computational domain, is straightforward to compute using the standard expansion of the field in the wavelet basis. Making the substitution yields

$$\int_\Sigma u(x)dx = \sum_k u^{0,k} \int_D \phi_{0,k}(x)dx + \sum_{j=1}\sum_{k\in S_j} d^{j,k} \int_D \phi_{j,k}(x)dx. \tag{26}$$

Given the integrals of the basis functions, we can easily compute the total amount of some quantity.

That each basis element is a scaled, translated version of the fundamental solution to the interpolation implies that, ignoring edges of the computational domain for the moment,

$$\int \phi_{j,k}(x)dx = \frac{\Delta x}{2^j}\int \phi(x)dx. \tag{27}$$

The prefactor takes into account the difference in spacing for the two functions. The fundamental solution is defined for a spacing of 1. It is straightforward to show that the integral of the fundamental solution is 1 by defining a sequence of approximations to the integral using Riemann sums:

$$I_{(j)} = \sum_k \frac{1}{2^j}\phi(x^{j,k}). \tag{28}$$

The interpolation property of the fundamental solution makes it easy to show that $I_{(j)} = I_{(j+1)}$. Then, given the starting point that $I_{(0)} = 1$ we have that

$$\int \phi(x)dx = \lim_{j\to\infty} I_{(j)} = 1. \tag{29}$$

Thus,

$$\int \phi_{j,k}(x)dx = \frac{\Delta x}{2^j}. \tag{30}$$

We can use this in the expansion of the field to write

$$\int_\Sigma u(x)dx = \sum_k u^{0,k}\Delta x + \sum_{j=1}\sum_{k\in S_j} d^{j,k}\frac{\Delta x}{2^j}. \tag{31}$$

This expression allows the monitoring of the conserved quantities during the simulation. In every case examined, the conservation is good to the level of the chosen ϵ.

Near the edges of the computational grid, the basis elements no longer have unit integrals. To compute these integrals, it is necessary to make use of the two-scale relation for the basis to compute partial integrals:

$$I_a^b \equiv \int_a^b \phi(x)dx \tag{32}$$

where a, b are integers, one of which might be infinite. Some are simple, $I_0^\infty = 0.5$ due to the symmetry of the basis, but others require setting up a linear system using the two-scale relation. Once the set of partial integrals is computed, the basis elements near the edges are written as the sum of an extended basis that stretches past the edge of the computational domain. It is an exercise in algebra to show that each of the original basis elements modified by the edges can be written as a sum of these extended basis elements. The extended basis elements are again translated, scaled versions of the fundamental solution, so we can use the partial integrals for only the interval inside the original domain to compute the integral of the original basis elements. For the case of $p = 4$, with superscripts labeling the location in the grid, we find that

$$I_j^0 = \frac{121}{360}\frac{\Delta x}{2^j} \qquad I_j^1 = \frac{462}{360}\frac{\Delta x}{2^j}$$
$$I_j^2 = \frac{303}{360}\frac{\Delta x}{2^j} \qquad I_j^3 = \frac{374}{360}\frac{\Delta x}{2^j}. \tag{33}$$

Similar expressions hold at the largest k values.

In multiple dimensions, because the basis functions are simple products, the integral of the basis is just the product of the integrals in each direction.

2.5. *Fluid Methods*

As mentioned in the introduction, one goal of this project is to develop a fully relativistic fluid code to study the binary mergers of compact objects. This involves solving both the Einstein equations of general relativity for the spacetime geometry and coordinate conditions, and the relativistic fluid equations for an arbitrary geometry. With neutron star binary mergers as our model problem, we choose a numerical algorithm that satisfies the following conditions: (1) The fluid density and pressure in a neutron star spans several orders of magnitude, and ejecta from the stars can reach speeds near the speed of light, so we choose a robust high-resolution shock-capturing method. (2) The proper calculation of normal modes for neutron stars requires high-order reconstruction methods for the fluid variables so we implement both PPM and MP5 reconstructions. (3) The calculation of characteristic variables is computationally intensive for relativistic fluids, especially for relativistic MHD, so we choose a central scheme with an approximate Riemann solver. (4) The Einstein equations—fundamentally equations for classical fields often written in a second-order formulation—are most naturally discretized using finite differences so we choose a finite-difference fluid method to simplify coupling the two sets of equations.

In this section we assume a uniform grid of points labeled with an index, i.e., $x_j = x_{\rm min} + j\Delta x$, and a function evaluated at point x_j has the shorthand notation $f_j = f(x_j)$.

Our numerical method for solving the fluid equations is based on the finite-difference Convex ENO (CENO) scheme of Liu and Osher for conservation laws (Liu and Osher 1998). For simplicity we present the method for a one-dimensional problem. The extension to multiple dimensions is done by differencing each dimension in turn, as discussed in Section 2.6. We write the conservation law in semi-discrete form as

$$\frac{{\rm d}\mathbf{u}_i}{{\rm d}t} = -\frac{\Delta t}{\Delta x}\left(\hat{\mathbf{f}}_{i+1/2} - \hat{\mathbf{f}}_{i-1/2}\right), \tag{34}$$

where $\hat{\mathbf{f}}_{i+1/2}$ is a consistent numerical flux function

$$\hat{\mathbf{f}}_{i+1/2} = \hat{\mathbf{f}}(\mathbf{u}_{i-k}, \ldots, \mathbf{u}_{i+m}) \tag{35}$$

$$\mathbf{f}(\mathbf{u}) = \hat{\mathbf{f}}(\mathbf{u}, \ldots, \mathbf{u}). \tag{36}$$

Liu and Osher base the CENO method on the local Lax-Friedrichs (LLF) approximate Riemann solver, and they use a ENO interpolation scheme to calculate the numerical flux functions $\mathbf{f}_{i+1/2}$. In previous work we have found that the CENO scheme is too dissipative to reproduce the normal modes of neutron stars (Anderson et al. 2006), so we use the HLLE numerical flux (Harten et al. 1983; Einfeldt 1988) in place of LLF, and we use higher-order finite volume reconstruction methods, such as PPM (Colella and Woodward 1984) and MP5 (Suresh and Huynh 1997).

The numerical flux $\hat{\mathbf{f}}_{i+1/2}$ requires the fluid state at $\mathbf{u}_{i+1/2} = \mathbf{u}(x_{i+1/2})$. We use the fluid variables near this point to reconstruct both left and right states at the midpoint, $\mathbf{u}^{\ell}_{i+1/2}$ and $\mathbf{u}^{r}_{i+1/2}$, respectively. The numerical flux can then be written in terms of these new states as $\mathbf{f}_{i+1/2} = \mathbf{f}(\mathbf{u}^{\ell}_{i+1/2}, \mathbf{u}^{r}_{i+1/2})$. We have implemented piece-wise linear (TVD) reconstruction, the Piece-wise Parabolic Method (PPM), and MP5 reconstruction. The MP5 reconstruction method usually gives superior results compared to the other methods, so we have used this reconstruction for all tests in this paper, except for Case IV below. As we use a central scheme for the approximate Riemann solver, we reconstruct each fluid variable separately. Moreover, given the difficulty of calculating primitive variables (ρ, v^i, P) from the conserved variables (D, S_i, τ), we reconstruct the primitive variables (ρ, v^i, P), and then calculate corresponding conserved variables.

The MP5 method is a polynomial reconstruction of the fluid state that preserves monotonicity (Suresh and Huynh 1997; Mösta et al. 2014). It preserves accuracy near extrema and is computationally efficient. The reconstruction of a variable q proceeds in two steps. We first calculate an interpolated value for the state $q^{\ell}_{i+1/2}$, called the original value. In the second step, limiters are applied to the original value to prevent oscillations, producing the final limited value. The original value at the midpoint is

$$q^{\ell}_{i+1/2} = \frac{1}{60}\left(2q_{i-2} - 13q_{i-1} + 47q_i + 27q_{i+1} - 3q_{i+2}\right). \tag{37}$$

We then compute a monotonicity-preserving value

$$q^{MP} = u_i + {\rm minmod}(q_{i+1} - q_i, \tilde{\alpha}(q_i - q_{i-1})), \tag{38}$$

where $\tilde{\alpha}$ is a constant which we set as $\tilde{\alpha} = 4.0$. The minmod function gives the argument with the smallest magnitude when both arguments have the same sign

$${\rm minmod}(x, y) = \frac{1}{2}\left({\rm sgn}\,(x) + {\rm sgn}\,(y)\right){\rm min}\left(|x|, |y|\right). \tag{39}$$

The limiter is not applied to the original value when

$$(q^{\ell}_{i+1/2} - q_i)(q^{\ell}_{i+12} - q^{MP}) \leq \varpi|q|, \tag{40}$$

where $\varpi = 10^{-10}$ and $|q|$ is the L_2 norm of q_i over the stencil points $\{q_{i-2}, \ldots, q_{i+2}\}$. The $|q|$ factor does not appear in the original algorithm, but we follow Mösta et al. (2014) in adding this term to account for the wide range of scales in the different fluid variables.

When condition Eq. (40) does not hold, we apply a limiter to the original value. We then compute the second derivatives

$$D^{-}_i = q_{i-2} - 2q_{i-1} + q_i \tag{41}$$

$$D^{0}_i = q_{i-1} - 2q_i + q_{i+1} \tag{42}$$

$$D^{+}_i = q_i - 2q_{i+1} + q_{i+2}, \tag{43}$$

and

$$D^{M4}_{i+1/2} = {\rm minmod}(4D^0_i - D^+_i, 4D^+_i - D^0_i, D^0_i, D^+_i) \tag{44}$$

$$D^{M4}_{i-1/2} = {\rm minmod}(4D^0_i - D^-_i, 4D^-_i - D^0_i, D^0_i, D^-_i). \tag{45}$$

The minmod function is easily generalized for an arbitrary number of arguments as

$${\rm minmod}(z_1, \ldots, z_k) = s\,{\rm min}\left(|z_1|, \ldots, |z_k|\right), \tag{46}$$

where

$$s = \frac{1}{2}\left(\mathrm{sgn}(z_1) + \mathrm{sgn}(z_2)\right) \times \left|\frac{1}{2}\left(\mathrm{sgn}(z_1) + \mathrm{sgn}(z_3)\right) \times \ldots \times \frac{1}{2}\left(\mathrm{sgn}(z_1) + \mathrm{sgn}(z_k)\right)\right|. \quad (47)$$

We then compute the following quantities

$$q^{UL} = q_i + \alpha\left(q_i - q_{i+1}\right) \quad (48)$$

$$q^{AV} = \frac{1}{2}\left(q_i + q_{i+1}\right) \quad (49)$$

$$q^{MD} = q^{AV} - \frac{1}{2}D^{M4}_{i+1/2} \quad (50)$$

$$q^{LC} = q_i + \frac{1}{2}\left(q_i - q_{i-1}\right) + \frac{4}{3}D^{M4}_{i-1/2}, \quad (51)$$

to obtain limits for an accuracy-preserving constraint

$$q_{\min} = \max\left(\min\left(q_i, q_{i+1}, q^{MD}\right), \min\left(q_i, q^{UL}, q^{LC}\right)\right) \quad (52)$$

$$q_{\max} = \min\left(\max\left(q_i, q_{i+1}, q^{MD}\right), \max\left(q_i, q^{UL}, q^{LC}\right)\right). \quad (53)$$

Finally, the limited value for the midpoint is

$$q^{\ell,\mathrm{Lim}}_{i+1/2} = q^{\ell}_{i+1/2} + \mathrm{minmod}\left(q_{\min} - q^{\ell}_{i+1/2}, q_{\max} - q^{\ell}_{i+1/2}\right). \quad (54)$$

To compute the right state $q^r_{i-1/2}$, we repeat the algorithm but reflect the stencil elements about the center, replacing $\{q_{i-2}, q_{i-1}, q_i, q_{i+1}, q_{i+2}\}$ with $\{q_{i+2}, q_{i+1}, q_i, q_{i-1}, q_{i-2}\}$.

The HLLE approximate Riemann solver is a central-upwind flux function that uses the maximum characteristic speeds in each direction to calculate a solution to the Riemann problem (Harten et al. 1983; Einfeldt 1988)

$$\hat{\mathbf{f}}^{\mathrm{HLLE}}_{i+1/2} = \frac{\lambda^+_r \mathbf{f}(\mathbf{u}^{\ell}_{i+1/2}) - \lambda^-_{\ell}\mathbf{f}(\mathbf{u}^{r}_{i+1/2})}{\lambda^+_r - \lambda^-_{\ell}} + \frac{\lambda^+_r\lambda^-_{\ell}(\mathbf{u}^{r}_{i+1/2} - \mathbf{u}^{\ell}_{i+1/2})}{\lambda^+_r - \lambda^-_{\ell}}, \quad (55)$$

where λ^+ and λ^- represent the largest characteristic speeds at the interface in the right and left directions, respectively.

The largest and smallest characteristic speeds of the relativistic fluid in flat spacetime in the direction x^i are

$$\lambda_{\pm} = \frac{1}{1 - v^2 c_s^2}\left\{v^i(1 - c_s^2) \pm \sqrt{c_s^2(1 - v^2)\left[\gamma^{ii}(1 - v^2 c_s^2) - v^i v^i (1 - c_s^2)\right]}\right\}, \quad (56)$$

where the sound speed c_s is

$$c_s^2 = \frac{1}{h}\left(\frac{\partial P}{\partial \rho}\right)\bigg|_{\epsilon} + \frac{P}{\rho^2 h}\left(\frac{\partial P}{\partial \epsilon}\right)\bigg|_{\rho}. \quad (57)$$

2.6. *Time Integration*

The conservation equations are written in semi-discrete form:

$$\frac{\mathrm{d}\mathbf{u}_{i,j,k}}{\mathrm{d}t} = -\frac{1}{\Delta x}\left(\hat{\mathbf{f}}^1{}_{i+1/2,j,k} - \hat{\mathbf{f}}^1{}_{i-1/2,j,k}\right) - \frac{1}{\Delta y}\left(\hat{\mathbf{f}}^2{}_{i,j+1/2,k} - \hat{\mathbf{f}}^2{}_{i,j-1/2,k}\right) - \frac{1}{\Delta z}\left(\hat{\mathbf{f}}^3{}_{i,j,k+1/2} - \hat{\mathbf{f}}^3{}_{i,j,k-1/2}\right) + \mathbf{s}\left(\mathbf{u}_{\mathbf{i}}\right) \quad (58)$$

where $\hat{\mathbf{f}}_{i+1/2}$ is the numerical flux. The flux functions in each direction are evaluated separately. The sparse wavelet representation leads to a scheme for integrating a system of differential equations in time by using the method of lines. The coefficients in the expansion become time dependent and can be integrated in time using any standard time integrator. In this work, the classical fourth-order Runge-Kutta method is used which has a CFL coefficient $\lambda_0 = 2/3$. The velocity and characteristic speeds of the fluid are bounded by the speed of light, so the time step $\lambda = c\Delta t/\Delta x$ is bounded by the CFL coefficient $\lambda \leq \lambda_0$.

As the physical state evolves during the simulation, the set of essential points will change. This means that the method needs to support the promotion of a point to becoming essential and the demotion of a point from being essential. To allow for such changes to the set of essential points, so-called *neighboring points* are added to the grid. These are those points adjacent to an essential point at the next finer level. In a sense, these points are sentinels waiting to become essential. Given that the points at level 0 are always essential, the points at level 1 will all be at least neighboring, and in this way, both the level 0 and level 1 grids will be fully occupied. Both neighboring and essential points participate in time integration and, for this reason, are called *active* points.

At the end of each timestep, every active point has its wavelet transformation computed. Essential points that no longer exceed the error threshold are demoted, and neighboring points that exceed the threshold are promoted. Neighboring points promoted to being essential points will thus require their own neighboring points at the next finer level. In this way, as the solution develops features on finer scales, the grid adapts, adding points to the grid exactly where the resolution is needed. Initially, the field values for a neighboring point can be taken from the initial conditions. Neighbors added after the initial time slice are given field values from the inverse wavelet transformation. That is, they are given a wavelet coefficient of zero, so their fields are equal to the interpolation from the previous level.

Finally, there is a third class of grid points, called *nonessential* points, that are required to fill out wavelet or other computational stencils of essential and neighboring points. Nonessential points do not participate in time integration and are given values via interpolation.

In practice, an upper limit on refinement, $j_{\max}$, must be specified. During an evolution, it can happen that the solution naturally attempts to refine past $j_{\max}$. There are two options in this case. The first is for the code to complain and die, and the second is for the code to complain and warn the user. Taking the former approach assures

that the error bounds implied by the chosen ϵ are not violated, because if the grid attempts to add a point at level $j_{\max}+1$ it is because the point is needed. However, if there is a discontinuity in the solution, no level of refinement will be sufficient to satisfy the refinement criterion. One possible solution to this problem is to smooth over discontinuities in initial data, and add some viscosity to prevent their formation during the simulation. However, we are interested in sharp features that develop during the simulation and it is for that reason that we use a fluid reconstruction and numerical flux function so as to allow for these sharp features. Thus, with a method that allows for discontinuities, we can never fully satisfy the refinement criterion if a discontinuity develops, and so the grid will want to refine forever. As a result, we take the practical step of limiting the maximum refinement level.

2.7. *Primitive Solver*

An important aspect of any relativistic hydrodynamics code is the inversion between the conserved and the primitive variables. Because the equations are written in conservation form, the conserved variables are the evolved variables. However, the primitive variables are needed as part of the calculation. For Newtonian fluids, this inversion from the conserved to the primitive variables is algebraic, can be done in closed form and results in a unique solution for the primitive variables provided the conserved variables take on physical values. Such is not the case in relativistic situations. As a result, a number of related procedures can be found in the literature to effect this inversion (Duez et al. 2005; Etienne et al. 2012; Noble et al. 2006). Due to its importance, we sketch our approach to performing the inversion.

For this discussion, we revert to the undensitized form of the conserved variables (D, S_i, τ). In terms of the fluid primitives (ρ, v^i, P), and for our chosen (Γ-law) equation of state (with $1 < \Gamma \leq 2$), the conserved variables are given by the undensitized version of Eqs. (7-9). The inversion can be reduced to a single equation for $x = hW^2/(\tau + D)$, namely,

$$-\left(x-\frac{\Gamma}{2}\right)^2+\frac{\Gamma^2}{4}-(\Gamma-1)\beta^2=(\Gamma-1)\,\delta\,\sqrt{x^2-\beta^2}, \quad (59)$$

where we have defined

$$\beta^2=\frac{S^2}{(\tau+D)^2}, \qquad \delta=\frac{D}{\tau+D}. \quad (60)$$

Note that the left hand side, call it $f(x)$, is a downward pointing quadratic while the right hand side includes the square root of another quadratic, $g(x) = x^2 - \beta^2$, which has roots $\pm|\beta|$. Solving for x amounts to finding the intersections of $f(x)$ and $(\Gamma-1)\delta\sqrt{g(x)}$. For a physical solution, $x > |\beta|$, the largest root of $g(x)$. Therefore, there is a single intersection bracketed by this root of $g(x)$ and the larger root of $f(x)$, namely $|\beta| < x < x^*$ where

$$x^*=\frac{\Gamma}{2}+\left[\frac{\Gamma^2}{4}-(\Gamma-1)\beta^2\right]^{1/2}. \quad (61)$$

That this root of $f(x)$ is real is guaranteed by the dominant energy condition, given here as $\beta^2 < 1$. Hence a unique solution to the primitive inversion exists in the pure hydrodynamics case provided the conserved variables satisfy this inequality. Using a straightforward Newton's method allows us to solve for the primitive variables in virtually every case. Occasionally, when the inequality is violated, rescaling β^2 to bring it within physical bounds is sufficient to allow the primitive solve to proceed to a solution.

3. ONE DIMENSIONAL TESTS

Lora-Clavijo et al. (2013) outlines a number of simple one-dimensional Riemann problems for relativistic hydrodynamics. Each of the four cases outlined was run with OAHU, and the results are reported below. In each case, the base grid was chosen to have $N = 10$, and we have varied both the maximum number of refinement levels and the value of ϵ. For each Riemann problem, we take the overall domain to be from $x = -1$ to $x = 1$ with the two states separated at $x = 0$. The primitive fields on each side of the problem for the four cases are given in Table 1.

Case		v	ρ	p
I	$x<0$	0	10	13.33
	$x>0$	0	1	10^{-6}
II	$x<0$	0	1	10^{-6}
	$x>0$	0	10	13.33
III	$x<0$	-0.2	0.1	0.05
	$x>0$	0.2	0.1	0.05
IV	$x<0$	0.999999	0.001	3.333×10^{-9}
	$x>0$	-0.999999	0.001	3.333×10^{-9}

Table 1
Initial state for four Riemann problems tested with OAHU. The simulated domain is the interval $x \in [-1, 1]$, and the separation between the left and right states is at $x = 0$.

In each case, the results obtained with OAHU match closely the exact solution. Figure 5 shows the results for Case I at $t = 0.8$ with $N = 10$, $j_{\max} = 10$ and $\epsilon = 10^{-5}$. The solution found by OAHU matches the exact solution extremely well. The final grid has adapted to the features that form during the simulation. The final state shown has only 324 points out of a possible 10,241 points, giving this simulation a very high effective resolution at a savings of over 96 percent.

The bottom right panel of Figure 5 gives the level of each point in the grid. This figure is characteristic of the refinement of the wavelet method. When the solution is smooth, there is very little refinement, and where the solution exhibits sharp features, the refinement proceeds to higher levels. For the very sharp features in this example, the refinement proceeds to the highest level allowed for the particular simulation. A discontinuity in the solution will generically refine as far as is allowed by the simulation. There is no smooth approximation at any resolution to a sharp transition.

It is interesting to explore how the quality of the solution depends on the maximum refinement level allowed and on the refinement criterion, ϵ. Figure 6 shows two close up views of features for Case I run for three different values of $j_{\max}$. In each case, $N = 10$ and $\epsilon = 10^{-5}$. The overshoot in the density for the $j_{\max} = 10$ case is not an artifact of the adaptive scheme we employ; when run at an equivalent resolution in unigrid ($N = 5120$

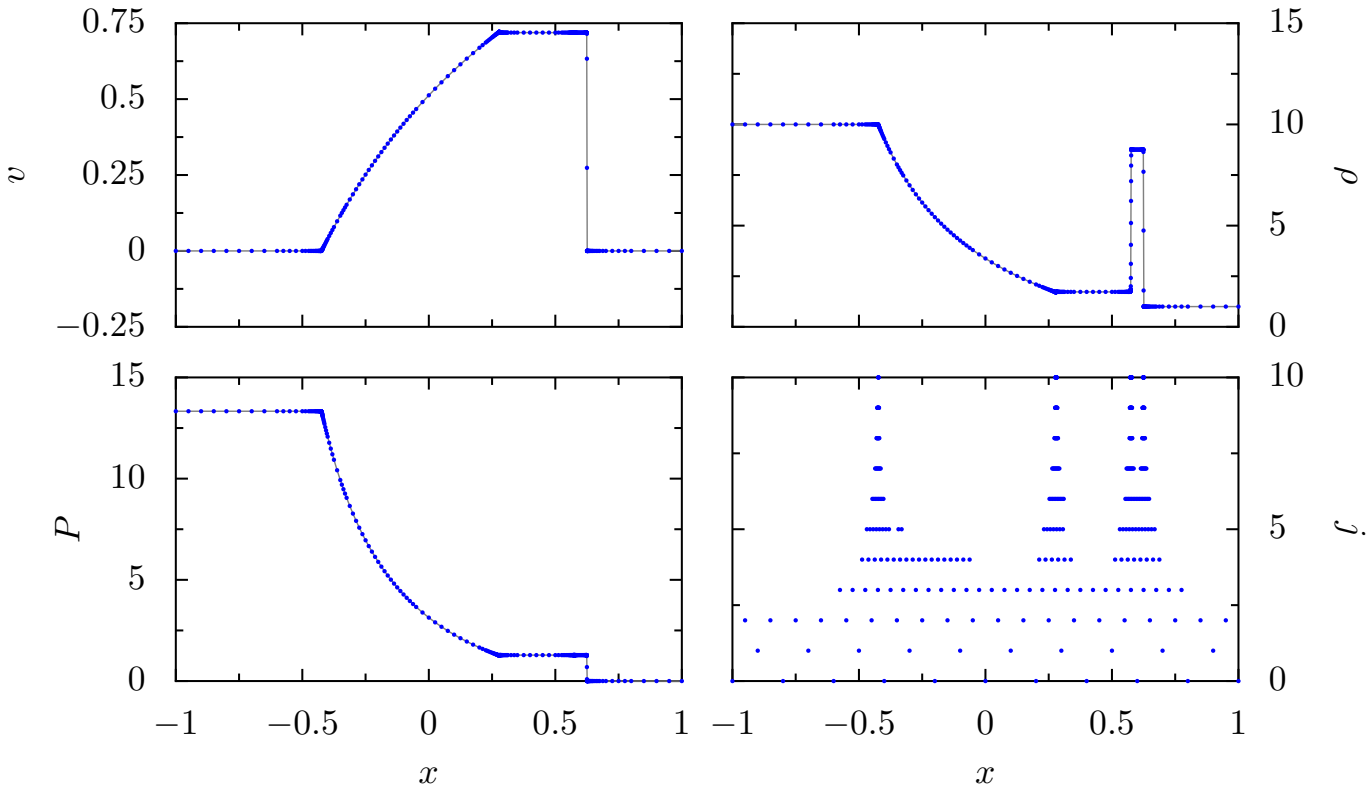

Figure 5. Comparison of the results from OAHU to the exact solution for the Case I Riemann problem (see Table 1). The solution (shown in gray) is at time $t = 0.8$. The positions of the wavelet grid points and their associated field values are shown in blue. This simulation was performed with $N = 10$, $j_{\max} = 10$ and $\epsilon = 10^{-5}$. The velocity, pressure and density all match the exact solution well. In the lower right panel the level of the point is plotted against the position of the point. The features in the profiles of v, P, and ρ match the location of refinement in the grid. The resulting wavelet grid is not hand-tuned; instead, it adapts to the evolution of the fluid. At the time shown, only 324 out of a possible 10241 grid points are occupied.

and $j_{\max} = 1$), the same overshoot is present. A similar close up is shown in Figure 7 giving a comparison of a set of runs with $N = 10$, $j_{\max} = 8$ and various values of ϵ. As ϵ decreases, the solution matches more closely the exact solution. However, there is little difference between $\epsilon = 10^{-4}$ and 10^{-5}. This demonstrates the interplay between $j_{\max}$ and ϵ. In this case, the sharpened refinement criterion would drive more refinement near this feature, but the maximum refinement level has already been reached.

Table 2 gives details of an error measure for each simulation:

$$L_2(f) = \frac{1}{N_{\rm occ}} \sqrt{\sum_{j,k} (f(x^{j,k}) - f_{ex}(x^{j,k}))^2}, \qquad (62)$$

where $N_{\rm occ}$ gives the number of occupied points, j and k index each point, $f(x)$ is the computed solution and $f_{ex}(x)$ is the exact solution. Increasing the maximum refinement level at the same ϵ tended to decrease the overall error. Similarly, as ϵ is decreased, the error decreases. Though, as indicated in Figure 7, the refinement is reaching its allowed maximum and so the additional refinement that would be generated by the smaller ϵ is not realized, leading only to modest accuracy gains. The much smaller errors for Case III are not surprising as this test contains two rarefaction waves and though there are sharp features in the exact solution, there are no discontinuities.

Case	$j_{\max}$	ϵ	$N_{\rm occ}$	$N_{\rm grid}$	$L_2(v)$ $[10^{-3}]$	$L_2(\rho)$ $[10^{-3}]$	$L_2(P)$ $[10^{-3}]$
I	6	10^{-5}	201	641	2.88	29.1	3.41
I	8	10^{-5}	261	2561	2.05	22.2	1.86
I	10	10^{-5}	324	10241	0.89	21.1	1.87
I	8	10^{-3}	145	2561	3.63	40.1	3.29
I	8	10^{-4}	215	2561	2.50	26.9	2.19
II	10	10^{-5}	320	10241	2.16	21.3	2.19
III	10	10^{-5}	422	10241	0.009	0.003	0.002
IV	10	10^{-5}	2759	10241	0.298	0.868	219

Table 2
Statistics for the Riemann problems presented in this work. $N_{\rm occ}$ gives the number of occupied grid points, while $N_{\rm grid}$ gives the maximum number of available points. The last three columns give the L_2-norms of the error of the velocity, density and pressure, as described in the text. Note that the MP5 reconstruction failed in Case IV, and so results using PPM reconstruction are given instead.

OAHU also monitors the conservation of the evolved variables during a simulation. For these test cases, the conservation is as good as the specified ϵ. This is to be expected as the representation keeps details only if those details are larger than ϵ. In each of the cases above, the relative drift in the conserved quantities is on the order of ϵ for that case.

4. RELATIVISTIC KELVIN-HELMHOLTZ INSTABILITY

We applied OAHU to the relativistic Kelvin-Helmholtz instability in two dimensions. For comparison, we have used identical initial conditions as in Radice and Rezzolla (2012). The computational domain is taken to be a peri-

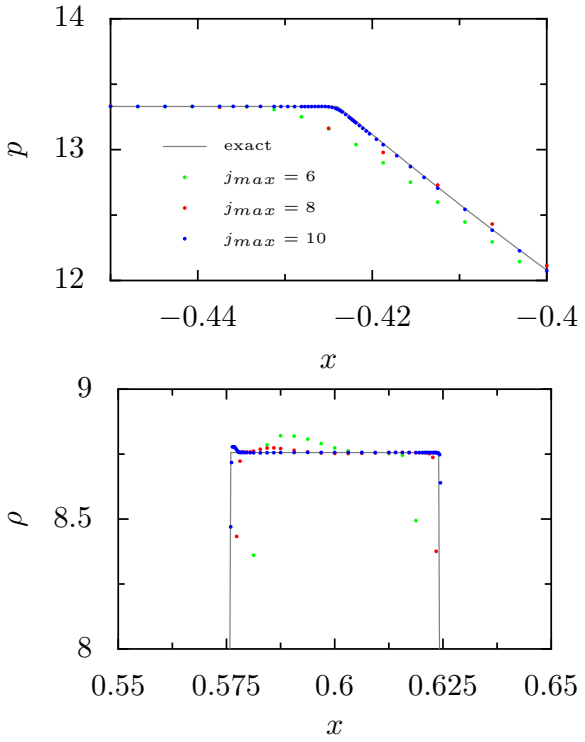

Figure 6. Detail of pressure at one end of the rarefaction wave (top) and the density in the shock (bottom) for Case I, with three different values of $j_{\max}$. As the maximum refinement level is increased, the wavelet solution matches the exact solution more closely.

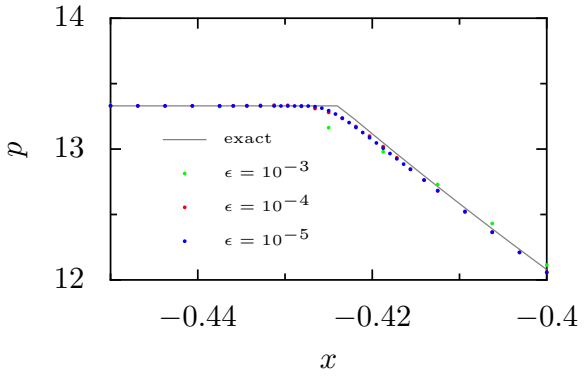

Figure 7. Detail of the pressure similar to the top panel of Figure 6, but with fixed $j_{\max} = 8$ and a varying ϵ. The refinement criterion has already pushed the refinement to the maximum level with $\epsilon = 10^{-4}$, and so there is little change as ϵ is decreased to 10^{-5}.

odic box from $x = -0.5$ to $x = 0.5$, and from $y = -1$ to $y = 1$. The shear is introduced via a counterpropagating flow in the x direction

$$v^x(y) = \begin{cases} V_s \tanh\left[(y-0.5)/a\right], & y > 0 \\ -V_s \tanh\left[(y+0.5)/a\right], & y \le 0. \end{cases} \tag{63}$$

Here $a = 0.01$ is the thickness of the shear layer and $V_s = 0.5$. A small perturbation of the velocity transverse to the shear layer seeds the instability:

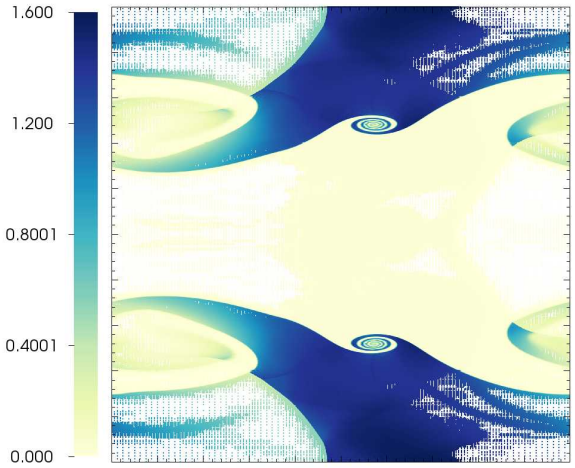

Figure 8. The relativistic Kelvin-Helmholtz instability at time $t = 3$. The points are colored by their density. This simulation used $(N_x, N_y) = (40, 80)$, $j_{\max} = 6$ and $\epsilon = 10^{-4}$. Compare with Radice and Rezzolla (2012).

$$v^y(x,y) = \begin{cases} A_0 V_s \sin(2\pi x) \exp\left[-(y-0.5)^2/\sigma\right], & y > 0 \\ -A_0 V_s \sin(2\pi x) \exp\left[-(y+0.5)^2/\sigma\right], & y \le 0, \end{cases} \tag{64}$$

where $A_0 = 0.1$, and $\sigma = 0.1$. For this test, $\Gamma = 4/3$ and the pressure is initially constant, $P = 1$. The density is given by a profile similar to v^x superposed on a constant as follows

$$\rho(y) = \begin{cases} \rho_0 + \rho_1 \tanh\left[(y-0.5)/a\right], & y > 0 \\ \rho_0 - \rho_1 \tanh\left[(y+0.5)/a\right], & y \le 0, \end{cases} \tag{65}$$

where $\rho_0 = 0.505$ and $\rho_1 = 0.495$.

Shown in Figure 8 is the density of this system at time $t = 3$ for a run having a base grid size of $(N_x, N_y) = (40, 80)$, and a maximum refinement level of $j_{\max} = 6$. Thus, the effective grid size is 2560×5120. The refinement criterion was $\epsilon = 10^{-4}$. The final state is consistent with the results in Radice and Rezzolla (2012). The conservation of the fluid is consistent with the chosen ϵ: D suffers a relative change of 6.13×10^{-6}, and τ suffers a relative change of 1.04×10^{-4}. Note the appearance of the secondary whirl along the shear boundary. In accord with the results of Radice and Rezzolla (2012), we find that the number and appearance of these secondary instabilities depend on the maximum resolution employed in our simulation, supporting their finding that these secondary instabilities are numerical artifacts.

5. RAYLEIGH-TAYLOR INSTABILITY IN A RELATIVISTIC OUTFLOW

One interesting problem in relativistic fluid dynamics is the interaction of a relativistic blast wave of ejecta from a GRB explosion with the surrounding ISM. As the shock expands adiabatically into the ISM, it loses thermal energy and eventually decelerates. This results in a double-shock system with a forward shock (traveling into the ISM), a contact discontinuity, and a reverse shock (moving into the ejecta). Levinson (2011) showed that the contact discontinuity is unstable to the Rayleigh-Taylor instability. The turbulence generated by this instability can amplify magnetic fields and the emission from the

thin shell of material behind the forward shock. Duffell and MacFadyen have studied this system with numerical simulations in a series of papers (Duffell and MacFadyen 2011, 2013, 2014), finding that the Rayleigh-Taylor instability can disrupt the forward shock for soft equations of state, which might be typical of radiative systems (Duffell and MacFadyen 2014).

Simulating the relativistic outflow of GRB ejecta constitutes an especially challenging numerical test for an adaptive relativistic fluid code. Relativistic effects compress the width of the thin shell by the Lorentz factor squared, $\Delta r/r \approx 1/W^2$. Capturing the Rayleigh-Taylor instability that forms at the contact discontinuity within the shell thus requires very high resolution within a thin shell that propagates outward with a velocity near the speed of light. Duffell and MacFadyen succeeded in simulating this system using an elegant moving mesh code, TESS (Duffell and MacFadyen 2011). The computational cells in TESS are allowed to move with the fluid, giving very high resolution in the shell and at the shocks. As a final test, we repeat the decelerating shock test here with OAHU to demonstrate the adaptive capability of the wavelet approach for relativistic hydrodynamics.

We use the initial data for the decelerating shock given in Duffell and MacFadyen (2011). The initial data are spherically symmetric, but this symmetry is broken by the instability, so we perform the simulation in cylindrical coordinates. We label these coordinates $\{s, z\}$, where s is the cylindrical radius, and the spherical radius r is given by $r^2 = s^2 + z^2$. The initial data for the spherical explosion are

$$\rho = \begin{cases} \rho_0 (r_0/r_{\rm min})^{k_0} & r < r_{\rm min} \\ \rho_0 (r_0/r)^{k_0} & r_{\rm min} < r < r_0 \\ \rho_0 (r_0/r)^{k} & r_0 < r, \end{cases} \tag{66}$$

where the different parameters are chosen to be

$$k_0 = 4, \quad r_0 = 0.1, \quad r_{\rm min} = 0.001. \tag{67}$$

A spherical explosion into a medium with a power-law dependence, $\rho \simeq r^{-k}$, will decelerate if $k < 3$. So we choose $k = \{0, 1, 2\}$ for our runs below. The pressure is given by

$$P = \begin{cases} e_0 \rho/3 \text{ for } r < r_{\rm exp} \\ 10^{-6} \rho \text{ for } r > r_{\rm exp}, \end{cases} \tag{68}$$

where $r_{\rm exp} = 0.003$ and the constant e_0 is chosen such that the outgoing shock has a Lorentz factor of $W \approx 10$. We set $e_0 = \{6, 4, 6\}$ for $k = \{0, 1, 2\}$, respectively.

Three different cases $k = \{0, 1, 2\}$ are simulated to $t = 0.8$, and the solutions at this time are shown in Figures 9, 10, 11. In each case, ten levels of refinement were used with a refinement criterion value of $\epsilon = 10^{-4}$. The Lorentz factor for the shock waves is ~ 12. All simulations were evolved in their entirety in 2-D from the initial conditions using the wavelet method described in this work. The results are consistent with those obtained with the TESS code. As k is increased, the width of the blast wave decreases. For $k = 0$ the RT instability is well resolved. For $k = 1$, the instability is evident, though with less detail than $k = 0$. In the $k = 2$ case, the width of the blast wave is too narrow to properly resolve the substructures in the instability. That there is an instability is apparent, but it lacks the definition of even the $k = 1$ case. These features could be resolved by increasing $j_{\rm max}$ for the $k = 2$ simulation. The conservation of all conserved variables was externally monitored throughout the simulation. Variation in the conservation of D amounted to less than 0.001% while variation in the conservation of τ was somewhat larger at 0.8%, visibly due to boundary effects along the z-axis.

6. SUMMARY

Motivated by the need to efficiently resolve the many emerging localized features and instabilities present in astrophysics simulations such as the merger of two neutron stars, this work has presented a wavelet based approach for solving the relativistic hydrodynamic equations. The resulting implementation of this approach, OAHU, has reproduced a number of results in relativistic hydrodynamics, including the one dimensional shock tube tests of Lora-Clavijo et al. (2013), the relativistic Kelvin-Helmholtz instability (Beckwith and Stone 2011; Radice and Rezzolla 2012), and the Rayleigh-Taylor instability resulting from a gamma ray burst outflow model (Duffell and MacFadyen 2011). Unlike adaptive mesh refinement based on nested boxes, the unstructured dyadic grid of collocation points in the wavelet approach conforms to highly localized solution features without creating the box-shaped numerical artifacts typically present in nested box adaptive mesh refinement simulations. Further, the approach presented here demonstrates the efficiency and utility of using the coefficients from the wavelet transformation to drive refinement without requiring problem specific *a priori* refinement criteria.

The wavelet method described here can be directly applied to the equations of relativistic magnetohydrodynamics (MHD) which describe a plasma of relativistic particles in the limit of infinite conductivity. Investigating MHD with wavelets will be part of future work.

For use in the merger simulations of astrophysical compact objects such as neutron stars and black holes, the wavelet based relativistic hydrodynamics kernel must be integrated with a kernel solving the Einstein equations for gravity. The wavelet method presented in this work has been designed expressly for this purpose and is a crucial feature for its use in astrophysics. The results from fully dynamic gravitational and hydrodynamics simulations as well as the method for integrating the hydrodynamics and gravitation computational kernels with the wavelet approach will be reported in future work.

Although not a focus of this work, the parallel implementation of the wavelet simulation framework presented here deviates from conventional practice in combining multi-threading with a form of message-driven computation sometimes referred to as asynchronous multi-tasking. The scalable asynchronous multi-tasking aspects of this work will be addressed in future work.

7. ACKNOWLEDGMENTS

It is a pleasure to thank our long-term collaborators Luis Lehner, Steven L. Liebling, and Carlos Palenzuela, with whom we have had many discussions on adaptive methods for relativistic hydrodynamics. We acknowledge

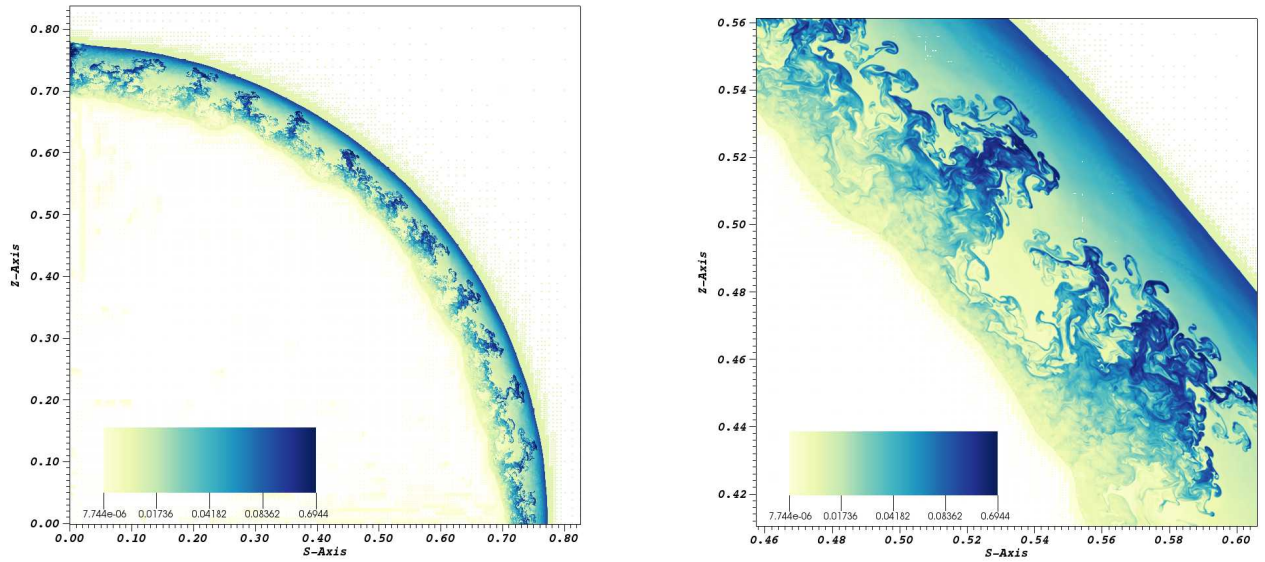

Figure 9. The $k = 0$ spherical explosion case with a decelerating relativistic shock and a mass excess. After a coasting period, the solution develops two shocks separated by a contact discontinuity unstable to the Rayleigh-Taylor instability. Results are shown at $t = 0.8$ for $j_{\max} = 10$ with $\epsilon = 10^{-4}$. This figure also demonstrates the adaptivity of the method; outside the blast wave there is little refinement, while inside the blast, the small scale features drive high levels of refinement, leading to a well-resolved Rayleigh-Taylor instability.

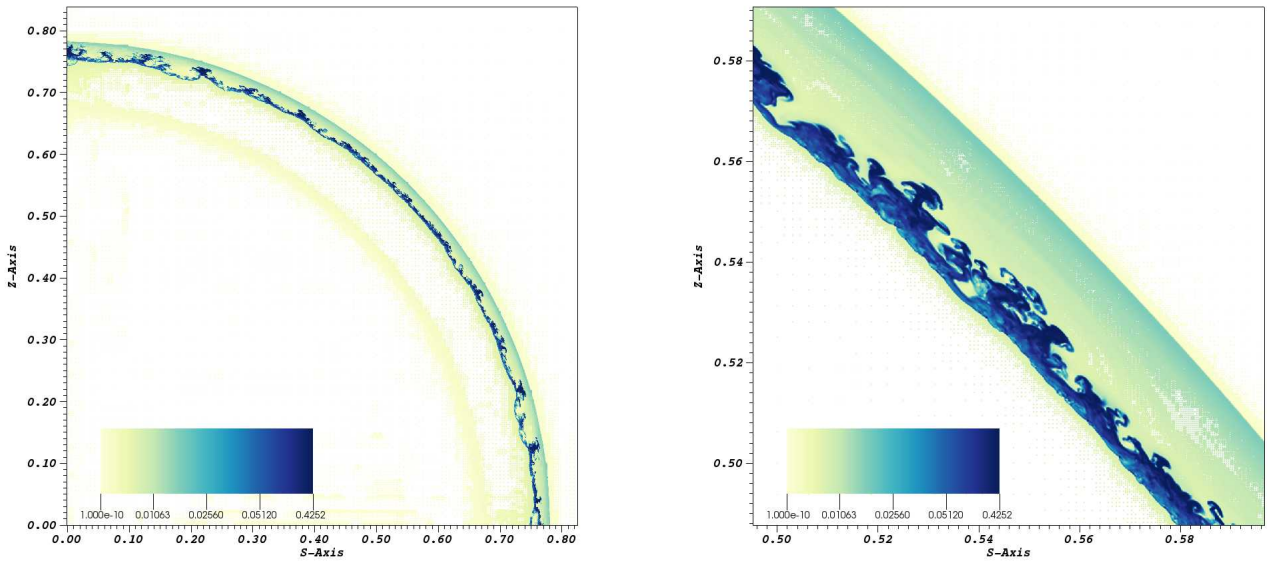

Figure 10. The $k = 1$ spherical explosion case with a decelerating relativistic shock and a mass excess. Results are shown at $t = 0.8$ for $j_{\max} = 10$ with $\epsilon = 10^{-4}$.

Thomas Sterling with whom we have had many discussions on the parallel implementation of OAHU. We also acknowledge many helpful discussions on wavelets with Temistocle Grenga and Samuel Paolucci. This material is based upon work supported by the Department of Energy, National Nuclear Security Administration, under Award Number DE-NA0002377, the Department of Energy under Award Number DE-SC0008809, the National Science Foundation under Award Number PHY-1308727, and NASA under Award Number BL-4363100.

REFERENCES

J. Abadie, B. P. Abbott, R. Abbott, M. Abernathy, T. Accadia, F. Acernese, C. Adams, R. Adhikari, P. Ajith, B. Allen, et al. Topical Review: Predictions for the rates of compact binary coalescences observable by ground-based gravitational-wave detectors. *Classical and Quantum Gravity*, 27(17):173001, September 2010.

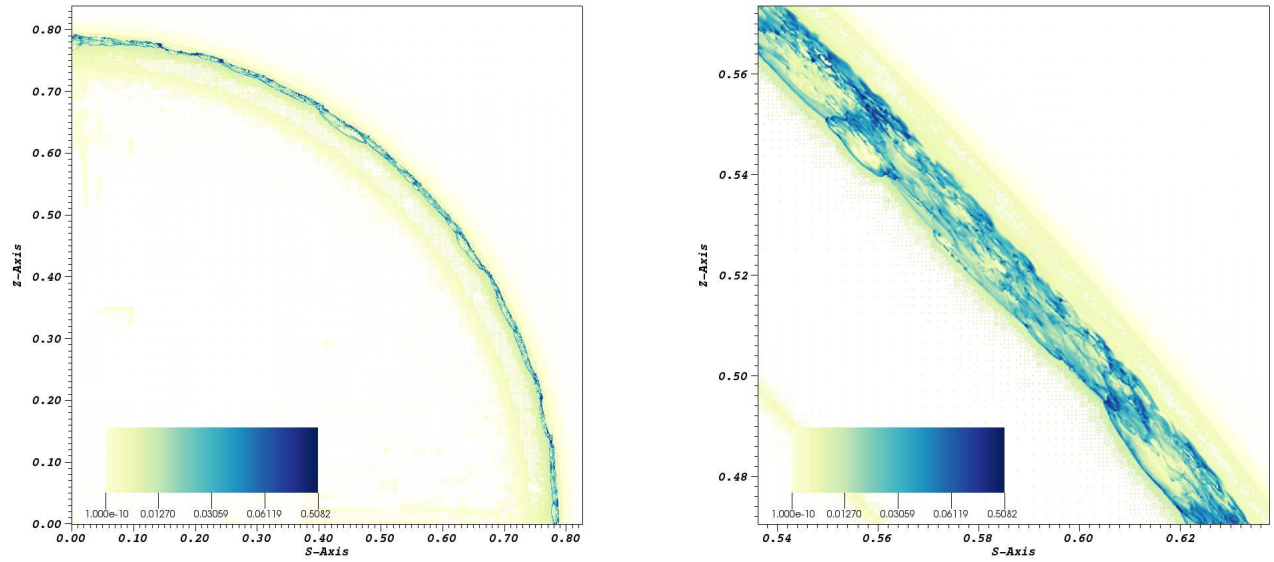

Figure 11. The $k = 2$ spherical explosion case with a decelerating relativistic shock and a mass excess. Results are shown at $t = 0.8$ for $j_{\max} = 10$ with $\epsilon = 10^{-4}$.

J. M. Alam, N. K.-R. Kevlahan, and O. V. Vasilyev. Simultaneous space-time adaptive wavelet solution of nonlinear parabolic differential equations. *J. Comput. Phys.*, 214(2): 829–857, 2006.

B. Alpert, G. Beylkin, R. Coifman, and V. Rokhlin. Wavelet-like bases for the fast solution of second-kind integral equations. *SIAM J. Sci. Comput.*, 14:159–184, 1993.

B. Alpert, G. Beylkin, D. Gines, and L. Vozovoi. Adaptive solution of partial differential equations in multiwavelet bases. *J. Comput. Phys.*, 182:149–190, 2002.

M. Anderson, E. W. Hirschmann, S. L. Liebling, and D. Neilsen. Relativistic MHD with adaptive mesh refinement. *Class. Quant Grav.*, 23:6503–6524, 2006.

K. Beckwith and J. M. Stone. A second-order Godunov method for multi-dimensional relativistic magnetohydrodynamics. *ApJS*, 193:6, 2011.

E. Berger. Short-duration gamma-ray bursts. *arXiv:1311.2603*, 2013.

M. J. Berger and J. Oliger. Adaptive mesh refinement for hyperbolic partial differential equations. *J. Comp. Phys.*, 53: 484, 1984.

S. Bertoluzza and G. Naldi. A wavelet collocation method for the numerical solution of partial differnetial equations. *Appl. Comput. Harmon. A.*, 3:1–9, 1996.

G. Beylkin. On the representation of operators in bases of compactly supported wavelets. *SIAM J. Numer. Anal.*, 6: 1716–1740, 1992.

G. Beylkin and N. Coult. Multiresolution strategy for reduction of elliptic pdes and eigenvalue problems. *Appl. Comput. Harmon. A.*, 5:129–155, 1998.

S. Chawla et al. Mergers of magnetized neutron stars with spinning black holes: Disruption, accretion and fallback. *Phys. Rev. Lett.*, 105:111101, 2010.

N. Chegini and R. Stevenson. Adaptive wavelet schemes for parabolic problems: Sparse matrices and numerical results. *SIAM. J. Numer. Anal.*, 49:182–212, 2011.

P. Colella and P. R. Woodward. The piecewise parabolic method (PPM) for gas dynamical simulations. *J. Comput. Phys.*, 54: 174–201, 1984.

W. Dahmen, A. Kurdila, and P. Oswald. *Multiscale wavelet methods for partial differential equations*. Academic Press, 1997.

G. Deslauriers and S. Dubuc. Symmetric iterative interpolation processes. *Constr. Approx.*, 5:49–68, 1989.

D. L Donoho. Interpolating wavelet transforms. *Preprint, Department of Statistics, Stanford University*, 2, 1992.

M. D. Duez, Y. T. Liu, S. L. Shapiro, and B. C. Stephens. Excitation of MHD modes with gravitational waves: A testbed for numerical codes. *Phys. Rev.*, D72:024029, 2005.

P. C. Duffell and A. I. MacFadyen. TESS: A Relativistic Hydrodynamics Code on a Moving Voronoi Mesh. *Astrophys. J. Suppl.*, 197:15, 2011. doi:10.1088/0067-0049/197/2/15.

P. C. Duffell and A. I. MacFadyen. Rayleigh-Taylor Instability in a Relativistic Fireball on a Moving Computational Grid. *Astrophys. J.*, 775:87, 2013. doi:10.1088/0004-637X/775/2/87.

P. C. Duffell and A. I. MacFadyen. Shock Corrugation by Rayleigh-Taylor Instability in GRB Afterglow Jets. *Astrophys. J.*, 791:L1, 2014. doi:10.1088/2041-8205/791/1/L1.

B. Einfeldt. On Godunov-type methods for gas dynamics. *SIAM J. Numer. Anal.*, 25:294–318, 1988.

Z. B. Etienne, Y. T. Liu, V. Paschalidis, and S. L. Shapiro. General relativistic simulations of black hole-neturon star mergers: Effects of magnetic fields. *Phys. Rev.*, D85:064029, 2012.

F. Foucart, L. Buchman, M. D. Duez, M. Grudich, L. Kidder, et al. First direct comparison of nondisrupting neutron star-black hole and binary black hole merger simulations. *Phys.Rev.*, D88(6):064017, 2013.

R. Glowinski, W. Lawton, M. Ravachol, and E. Tenenbaum. Wavelet solution of linear and nonlinear elliptic, parabolic and hyperbolic problems in one space dimension. Technical report, Aware Inc., 1989.

A. Harten, P. D. Lax, and B. van Leer. On upstream differencing and Godunov-type schemes for hyperbolic conservation laws. *SIAM Rev.*, 25:35–61, 1983.

M. Holmström. Solving hyperbolic pdes using interpolating wavelets. *SIAM J. Sci. Comput.*, 21(2):405–420, 1999.

K. Hotokezaka, K. Kiuchi, K. Kyutoku, H. Okawa, Y.-i. Sekiguchi, M. Shibata, and K. Taniguchi. Mass ejection from the merger of binary neutron stars. *Phys. Rev. D*, 87(2): 024001, January 2013.

A. Kazemi Nasab, A. Kılıçman, Z. Pashazadeh Atabakan, and W. J. Leong. A numerical approach for solving singular nonlinear Lane-Emden type equations arising in astrophysics. *New A*, 34:178–186, 2015.

K. Kiuchi, K. Kyutoku, Y. Sekiguchi, M. Shibata, and T. Wada. High resolution numerical-relativity simulations for the merger of binary magnetized neutron stars. *Phys.Rev.*, D90(4):041502, 2014.

A. Latto and E. Tenenbaum. Compactly supported wavelets and the numerical solution of Burger's equation. *C. R. Acad. SCi. Paris*, 311:903–909, 1990.

A. Levinson. Relativistic jets at high energies. *IAU Symp.*, 275: 24, 2011.

L. X. Li and B. Paczynski. Transient events from neutron star mergers. *Astrophys.J.*, 507:L59, 1998.

X-D Liu and S Osher. Convex ENO high order multi-dimensional schemes without field by field decomposition or staggered grids. *J. Comp. Phys.*, 142:304–330, 1998.

F. D. Lora-Clavijo, J. P. Cruz-Prez, F. S. Guzmn, and J. A. Gonzlez. Exact solution of the 1D Riemann problem in Newtonian and relativistic hydrodynamics. *Rev. Mex. Fis.*, E59:28–50, 2013.

F. Mertens and A. Lobanov. Wavelet-based decomposition and analysis of structural patterns in astronomical images. *A&A*, 574:A67, 2015.

P. Mösta, B. C. Mundim, J. A. Faber, R. Haas, S. C. Noble, T. Bode, F. Lffler, C. D. Ott., C. Reisswig, and E. Schnetter. GRHydro: A new open source general-relativistic magnetohydrodynamics code for the Einstein Toolkit. *Class. Quant. Grav.*, 31:015005, 2014.

S. C. Noble, C. F. Gammie, J. C. McKinney, and L. Del Zanna. Primitive variable solvers for conservative general relativistic magnetohydrodynamics. *Astrophys. J.*, 641:626–637, 2006.

C. Palenzuela, L. Lehner, M. Ponce, S. L. Liebling, M. Anderson, et al. Gravitational and electromagnetic outputs from binary neutron star mergers. 111:061105, 2013.

C. Palenzuela, S. L. Liebling, D. Neilsen, L. Lehner, O. L. Caballero, E. OConnor, and M. Anderson. Effects of the microphysical equation of state in the mergers of magnetized neutron stars with neutrino cooling. *Phys. Rev.*, D92(4): 044045, 2015.

S. Paolucci, Z. J. Zikoski, and T. Grenga. WAMR: An adaptive wavelet method for the simulation of compressible reacting flow. Part II. The parallel algorithm. *J. Comput. Phys.*, 272: 842 – 864, 2014a.

S. Paolucci, Z. J. Zikoski, and D. Wirasaet. WAMR: An adaptive wavelet method for the simulation of compressible reacting flow. Part I. Accuracy and efficiency of algorithm. *J. Comput. Phys.*, 272:814 – 841, 2014b.

J. Powell, D. Trifirò, E. Cuoco, I. S. Heng, and M. Cavaglià. Classification methods for noise transients in advanced gravitational-wave detectors. *Classical Quant. Grav.*, 32: 215012, 2015.

S. Qian and J. Weiss. Wavelets and the numerical solution of boundary value problems. *Appl. Math. Lett.*, 6:47–52, 1993a.

S. Qian and J. Weiss. Wavelets and the numerical solution of partial differential equations. *J. Comput. Phys.*, 106:155–175, 1993b.

D. Radice and L. Rezzolla. THC: a new high-order finite-difference high-resolution shock-capturing code for special-relativistic hydrodynamics. *A&A*, 547:A26, 2012.

J. D. Regele and O. V. Vasilyev. An adaptive wavelet-collocation method for shock computations. *Int. J. Comput. Fluid D.*, 23: 503–518, 2009.

S. Rosswog. Conservative, special-relativistic SPH. *J. Comp. Phys.*, 229:8591–8612, 2010.

Y. Sekiguchi, K. Kiuchi, K. Kyutoku, and M. Shibata. Dynamical mass ejection from binary neutron star mergers: Radiation-hydrodynamics study in general relativity. *Phys.Rev.*, D91(6):064059, 2015.

V. Springel. E pur si muove: Galilean-invariant cosmological hydrodynamical simulations on a moving mesh. *MNRAS*, 401: 791–851, 2010.

A. Suresh and H. T. Huynh. Accurate monotonicity-preserving schemes with runge-kutta time stepping. *J. Comput. Phys.*, 136:83–99, 1997.

K. Urban. *Wavelet methods for elliptic partial differential equations*. Oxford University Press, 2009.

M. M. Varughese, R. von Sachs, M. Stephanou, and B. A. Bassett. Non-parametric transient classification using adaptive wavelets. *MNRAS*, 453:2848–2861, 2015.

O. V. Vasilyev and C. Bowman. Second-generation wavelet collocation method for the solution of partial differential equations. *J. Comput. Phys.*, 165:660–693, 2000.

O. V. Vasilyev and S. Paolucci. A dynamically adaptive multilevel wavelet collocation method for solving partial differential equations in a finite domain. *J. Comput. Phys.*, 125:498–512, 1996.

O. V. Vasilyev and S. Paolucci. A fast adaptive wavelet collocation algorithm for multidimensional pdes. *J. Comput. Phys.*, 138:16–56, 1997.

O. V. Vasilyev, S. Paolucci, and M. Sen. A multilevel wavelet collocation method for solving partial differential equations in a finite domain. *J. Comput. Phys.*, 120:33 – 47, 1995.